

Figs. 3 and 4 show Pt species located randomly on the ceria surfaces (not embedded in the ceria), with no preference for specific facets.

Atom trapping should be broadly applicable as a method for preparing single-atom catalysts. The approach requires a supply of mobile atoms and a support that can bind the mobile species. Conditions that are conducive to Ostwald ripening, which normally is implicated in the degradation of catalysts (3), are ideal because mobile species are continually being generated. In our work, at the aging temperature of 800°C in air, mobile PtO₂ is rapidly emitted; the estimated lifetime is only a few seconds for a 5-nm Pt crystallite (24). Surface species such as hydroxyls and carbonates, which could prevent the trapping of mobile species, would have desorbed at high temperatures, providing a clean surface for the formation of covalent metal oxide bonds that are needed to stabilize single atoms. Trapping of atoms provides a plausible explanation for the role of ceria in slowing the rates of Ostwald ripening and may help to explain how other supports modify the rates of catalyst sintering.

REFERENCES AND NOTES

- G. W. Graham *et al.*, *Catal. Lett.* **116**, 1–8 (2007).
- M. H. Wiebenga *et al.*, *Catal. Today* **184**, 197–204 (2012).
- T. W. Hansen, A. T. Delariva, S. R. Challa, A. K. Datye, *Acc. Chem. Res.* **46**, 1720–1730 (2013).
- T. R. Johns *et al.*, *J. Catal.* **328**, 151–164 (2015).
- J. A. Kurzman, L. M. Misch, R. Seshadri, *Dalton Trans.* **42**, 14653–14667 (2013).
- C. B. Alcock, G. W. Hooper, *Proc. R. Soc. London Ser. A* **254**, 551–561 (1960).
- G. Cavataio *et al.*, *SAE Int. J. Fuels Lubr.* **2**, 204–216 (2009).
- Y.-F. Yu-Yao, J. T. Kummer, *J. Catal.* **106**, 307–312 (1987).
- J. G. McCarty, K.-H. Lau, D. L. Hildenbrand, *Stud. Surf. Sci. Catal.* **111**, 601–607 (1997).
- C. Carrillo *et al.*, *J. Phys. Chem. Lett.* **5**, 2089–2093 (2014).
- G. B. McVicker, R. L. Garten, R. T. K. Baker, *J. Catal.* **54**, 129–142 (1978).
- Y. Nagai *et al.*, *J. Catal.* **242**, 103–109 (2006).
- J. A. Farmer, C. T. Campbell, *Science* **329**, 933–936 (2010).
- J. H. Kwak *et al.*, *Science* **325**, 1670–1673 (2009).
- B. Qiao *et al.*, *Nat. Chem.* **3**, 634–641 (2011).
- W.-Z. Li *et al.*, *Nat. Commun.* **4**, 2481 (2013).
- T. R. Johns *et al.*, *ChemCatChem* **5**, 2636–2645 (2013).
- H.-X. Mai *et al.*, *J. Phys. Chem. B* **109**, 24380–24385 (2005).
- S. Agarwal *et al.*, *ChemSusChem* **6**, 1898–1906 (2013).
- T. Wu *et al.*, *J. Phys. Chem. Lett.* **5**, 2479–2483 (2014).
- A. Bruix *et al.*, *Angew. Chem. Int. Ed.* **53**, 10525–10530 (2014).
- A. Neitzel *et al.*, *J. Phys. Chem. C* **120**, 9852–9862 (2016).
- Z. L. Wang, X. Feng, *J. Phys. Chem. B* **107**, 13563–13566 (2003).
- See supplementary materials on Science Online.
- P. J. Berlowitz, C. H. F. Peden, D. W. Goodman, *J. Phys. Chem.* **92**, 5213–5221 (1988).
- R. Kopelelt *et al.*, *Angew. Chem. Int. Ed.* **54**, 8728–8731 (2015).
- M. Cargnello *et al.*, *Science* **341**, 771–773 (2013).
- M. Moses-DeBusk *et al.*, *J. Am. Chem. Soc.* **135**, 12634–12645 (2013).
- K. Ding *et al.*, *Science* **350**, 189–192 (2015).
- F. Dvořák *et al.*, *Nat. Commun.* **7**, 10801 (2016).

ACKNOWLEDGMENTS

Supported by NSF GOALI grant CBET-1438765 (J.J., H.X., S.R.C., A.K.D.), General Motors Global R&D (G.Q., S.O., and M.H.W.), U.S. Department of Energy grant DE-FG02-05ER15712 (A.T.D., E.J.P., A.K.D., X.L.P.H., and Y.W.), and the Center for Biorenewable Chemicals funded by NSF grant EEC-0813570 (H.X., H.P., and A.K.D.). This work made use of the JEOL JEM-ARM200CF at the University of Illinois at Chicago. We thank A. Nicholls for

recording the AC-STEM images and D. Kunwar for assistance in catalyst preparation.

SUPPLEMENTARY MATERIALS

www.sciencemag.org/content/353/6295/150/suppl/DC1
Materials and Methods

Figs. S1 to S14
Tables S1 to S3
References (31–35)

26 April 2016; accepted 13 June 2016
10.1126/science.aaf8800

ANIMAL ROBOTICS

Tail use improves performance on soft substrates in models of early vertebrate land locomotors

Benjamin McInroe,^{1*} Henry C. Astley,^{1*} Chaohui Gong,² Sandy M. Kawano,³ Perrin E. Schiebel,¹ Jennifer M. Rieser,¹ Howie Choset,² Richard W. Blob,⁴ Daniel I. Goldman^{1,5,†}

In the evolutionary transition from an aquatic to a terrestrial environment, early tetrapods faced the challenges of terrestrial locomotion on flowable substrates, such as sand and mud of variable stiffness and incline. The morphology and range of motion of appendages can be revealed in fossils; however, biological and robophysical studies of modern taxa have shown that movement on such substrates can be sensitive to small changes in appendage use. Using a biological model (the mudskipper), a physical robot model, granular drag measurements, and theoretical tools from geometric mechanics, we demonstrate how tail use can improve robustness to variable limb use and substrate conditions. We hypothesize that properly coordinated tail movements could have provided a substantial benefit for the earliest vertebrates to move on land.

During the vertebrate invasion of land, 385 to 360 million years ago, early tetrapods and relatives faced a variety of challenges (1), including locomotion in terrestrial environments. Terrestrial locomotion relies on interactions between the body and substrate to generate propulsive forces, but the interaction between the organism and some substrates may be complex. Fossil evidence indicates that tetrapods emerged from water in near-shore habitats, where they likely encountered flowable soft substrates such as sands and muds (2, 3). These substrates exhibit properties of solids and fluids, either jamming or yielding (plastic deformation of the material) depending on how they are loaded (4) and sloped (5).

The challenge of movement on flowable substrates therefore arises from the complexity of interactions between the substrate and the organism. Even on level deformable substrates, subtle variations in limb morphology (6) and kinematics (7) can lead to substantial differences in performance. Furthermore, interactions between appendages and these substrates leave

local disturbances, which can influence subsequent interactions, sometimes leading to deteriorating locomotor performance and eventual total locomotor failure (8). As substrate slope increases, yield forces decrease and downhill material flow becomes important, reducing the range of effective locomotor strategies (5).

The use of an additional locomotor structure that can be independently coordinated may allow a greater range of effective behaviors, even in the absence of derived limb morphology and sophisticated motor patterns. We propose that the tail could have been a critical locomotor structure for early tetrapods. In addition to being a primary driver of aquatic locomotion, tails play major roles in the propulsion of many modern fishes during terrestrial locomotion (9–12) and can be used as inertial reorientation appendages in some tetrapods (13, 14). Thus, the use of a prominent tail [as seen in fossil taxa (15–17) (Fig. 1A)] may have increased locomotor robustness to environmental and kinematic variables.

Evaluating locomotor performance for extinct taxa is challenging (18, 19), in part because the sensitivity of locomotion on complex substrates to kinematics and control strategies cannot necessarily be inferred from range of motion and morphology (7). Therefore, to test our hypothesis, we used three complementary modeling methods (Fig. 1): a model organism, a robophysical model, and a mathematical model. We made several choices governing our modeling approaches. In our locomotors, we modeled symmetrical, forelimb-driven

¹School of Physics, Georgia Institute of Technology, Atlanta, GA, USA. ²Robotics Institute, Carnegie Mellon University, Pittsburgh, PA, USA. ³National Institute for Mathematical and Biological Synthesis, University of Tennessee, Knoxville, TN, USA. ⁴Department of Biological Sciences, Clemson University, Clemson, SC, USA. ⁵School of Biology, Georgia Institute of Technology, Atlanta, GA, USA.

*These authors contributed equally to this work. †Corresponding author. Email: daniel.goldman@physics.gatech.edu

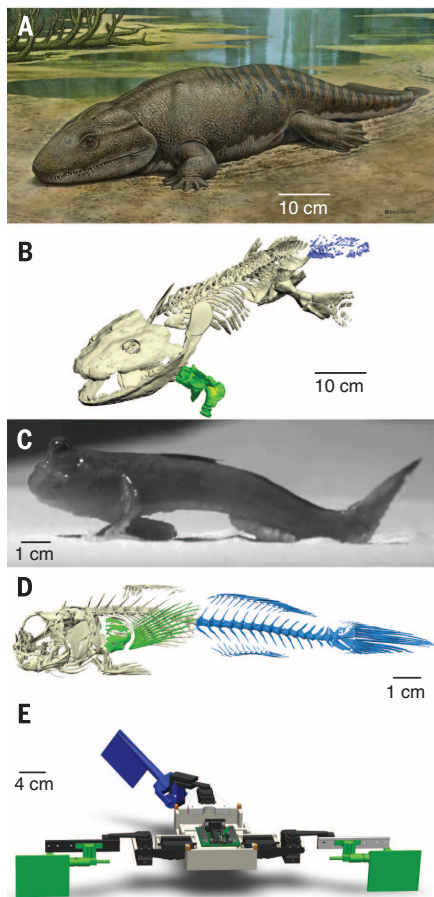


Fig. 1. Target and model systems for understanding early tetrapod locomotion on granular media.

(A) A reconstruction of *Ichthyostega* (~360 million years ago), an example of an early tetrapod body plan, by Raul Martin. (B) Skeletal reconstruction of *Ichthyostega*, an example of an early tetrapod body plan [from (20)], highlighting the pectoral limbs (green) and tail (blue). (C) The mudskipper (*Periophthalmus barbarus*), a biological model for early terrestrial locomotors. (D) A micro-computed tomography scan reconstruction of a mudskipper skeleton, highlighting the pectoral fin (green) and tail (blue). (E) The MuddyBot, a 3D printed robot developed to model the locomotion of crutching early tetrapods. Limbs are in green and the tail is in blue.

crutching locomotion (rather than salamander-like movement) in accordance with recent studies of *Ichthyostega* (20, 21); this choice enabled simplicity of control (coordinating two appendages rather than four) and obviated the need for continuous, stable support of an elevated body. We note that we are not strictly modeling *Ichthyostega*, nor any specific fossil taxon associated with the water-land transition, but are instead seeking general principles underlying limbed, crutching locomotion on yielding media.

Our biological model is the mudskipper (*Periophthalmus barbarus*) (12, 18, 20–24), a small fish that frequently moves terrestrially using synchronous motions of the pectoral fins, although these animals can use their tails for rapid jumping

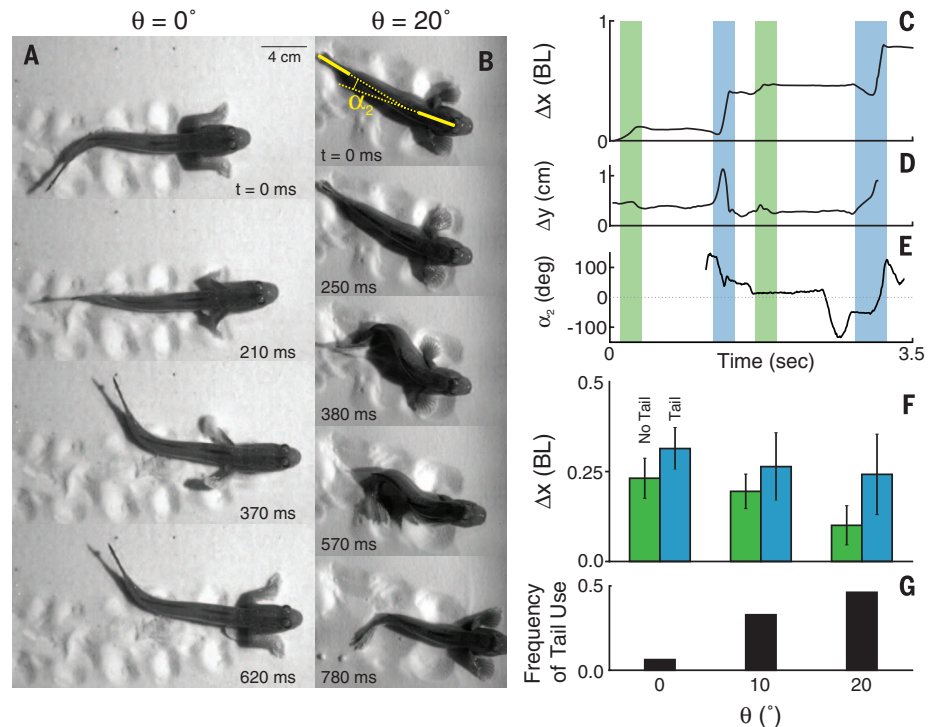


Fig. 2. Mudskipper locomotion on granular media at different substrate inclines (θ). (A and B) Dorsal-view video frames of a mudskipper fish on dry, loose sand inclined at 0° (A) and 20° (B) (movies S1 and S2). Yellow solid lines along the longest tail fin ray and from between the eyes to the anterior edge of the dorsal fin are used to compute the tail angle (α_2) in (E). The tail is not used propulsively in (A), although it moves slightly; in (B), the tail is used for propulsion. (C to E) Horizontal forward displacement per cycle (Δx) in body lengths (BL) for a single trial (C), vertical displacement (Δy , measured from eye) (D), and tail angle (α_2) (E) of mudskippers on sand at 20° incline. Cycles without tail use are indicated by green regions; cycles with tail use are indicated by blue regions (determined from video inspection). Missing values of α_2 are when the tail fin was out of view. (F) Δx at all inclines (θ) for steps without (green) and with (blue) tail use. Error bars denote SD. (G) Percentage of cycles with propulsive tail use across substrate inclines.

despite unspecialized tail morphology (25). Our robophysical model (Fig. 1E) (26) was designed with morphology representing the simplest possible version of a crutching locomotor, allowing us to systematically explore performance over a range of locomotor movements, including those movements not used by our biological model. Our mathematical model relies on the framework of geometric mechanics (27, 28) and allows us to understand how certain aspects of performance relate to coordination of limbs and tail. Our use of dry granular media was another modeling choice: The first vertebrates to move on land likely did so in wet shoreline habitats (such as mudflats) with properties that differ from those of dry granular media, but these media are united in displaying plastic deformation once the yield stress is exceeded (29–31). Although partially wet soils can display cohesion that increases yield stresses and results in larger “memory” effects, these rheological similarities [combined with the difficulty of preparing large volumes of standardized wet granular media (30)] led us to use dry media to model flowable substrates in our trials (30, 31).

Mudskippers ($N = 6$) were capable of effective locomotion over a level ($\theta = 0^\circ$) granular substrate [loose-packed dry oolite sand (table S1)]

using a crutching gait actuated by synchronous retraction of the pectoral fins with the tail angle (α_2) almost straight ($21^\circ \pm 22^\circ$; all measurements are means \pm SD) (Fig. 2A and movie S1), moving an average forward distance per cycle (Δx) of 0.21 ± 0.03 body lengths (BL) (Fig. 2F). During locomotion, mudskippers were able to fold the fin rays of the caudal and anal fins away from the substrate, allowing terrestrial locomotion without damage to or interference from these structures (Fig. 2B).

In some locomotor cycles, mudskippers used their tails (Fig. 2B and movie S2), bending the tail and planting the distal end of the tail and fin rays in the sand approximately orthogonal to the body axis ($119^\circ \pm 21^\circ$) (Fig. 2E) before retracting the pectoral fins and straightening the tail during the propulsive phase (Fig. 2B). Tracks left by these trials typically consisted of a series of paired impressions from the pectoral fins (sometimes obscured by yielding flow from subsequent steps, especially on inclines), with tail use leaving an additional impression offset to the right or left and overlapping the previous fin impressions (Fig. 2, A and B, and movies S1 and S2). Steps using the tail resulted in a higher displacement of 0.28 ± 0.08 BL on horizontal media (Fig. 2, C, D, and F).

As substrate incline angle increased, crutching with only the pectoral fins became less effective (Fig. 2F) and the frequency of steps for which the tail was used propulsively increased, from 6% on level substrate to 36% on substrate inclined at 10° and to 55% on substrate inclined at 20° (Fig. 2G). In addition to increasing displacement per cycle, tail use prevented downhill slip on inclined media when the tail was planted. The disparity in forward displacement increased between steps with and without tail use as substrate angle increased (Fig. 2F). At a 10° incline, mudskippers moved forward an average of 0.16 ± 0.03 BL with each step, versus 0.18 ± 0.08 BL when the tail was used (Fig. 2F). When the substrate was inclined to 20°, displacement was 0.07 ± 0.03 BL without tail use, increasing to 0.14 ± 0.07 BL with tail use (Fig. 2F). Further, mudskippers would occasionally jump clear of the test arena via tail-powered movements, indicating that the use of tails during crutching locomotion is controlled and submaximal.

A robophysical model of a crutching locomotor with limbs (Fig. 3A) allowed systematic testing of how locomotor performance in realistic granular environments was affected by variations in foot placement, limb adduction, and tail use (7). We elected to use a highly simplified morphology (a pair of laterally positioned, synchronously moving forelimbs and a posterior tail) (Fig. 3A) in order to focus on overarching locomotor control principles (“templates”) as opposed to the details of their anatomical implementation (“anchors”) (32). Although this model is simplified, it possesses some of the degrees of freedom seen in the mudskippers, namely the ability to control both body lifting (via limb adduction) and the interface with the substrate (limb supination) as well as use of the tail.

In addition to varying the incline ($\theta = 0^\circ$, 10° , and 20°) of the granular material, we varied three parameters of the robot: limb adduction angle (ψ), limb supination angle (ϕ), and presence or absence of tail use (Fig. 3). Adduction angle and the resultant lifting of the body is known to affect locomotor performance in similar robots on granular media (8) and may have been critical to terrestrial locomotion in early tetrapods (20). Supination angle, a simplified model of differences in limb placement, varied from a vertical limb insertion into the media (0°) to nearly flat (60°) in 15° increments. The tail was either used or not used (resulting in the posterior portion of the robot dragging in the media). In all cases, tail use induced alternating lateral rotations and displacements; although these yaw movements were often small ($<10^\circ$), they explain the few instances in which tail use was detrimental. To prevent damage to the motors, instead of sand we used two granular materials, loosely packed poppy seeds and spherical plastic particles (table S1) (33); prior work has shown that these substrates function well as models of more natural granular media (8, 33). Although the robot’s movements were slower than those of the mudskippers, all three substrates showed no dependence of force on speed over the ranges observed (~ 5 to 10 cm/s) (fig. S6).

In each trial, the robot performed a total of six limb cycles, the maximum number possible for the size of the bed. Insufficient first-step displacement has been shown to produce interactions with the previously disturbed media, resulting in lower displacement and further interactions until complete failure (stranding) (8). Conversely, if the first step is sufficient to prevent this interaction, the likelihood of failure decreases. In our experiments, few configurations produced intermediate displacements that led to decaying performance; most were either consistently successful or immediate failures (fig. S1). These trials were not sufficiently numerous to determine whether tail use altered the rate of decay, although it may do so indirectly if it increases first-step displacement. Consequently, we present data for only the first step (Δx_1).

To characterize how the adduction, supination, and tail use parameters affected the robot’s locomotion in undisturbed media, we measured Δx_1 for three trials per configuration (Fig. 3, D and E). During these trials, high values of adduction (which resulted in lifting much of the body clear of the substrate) and use of the tail improved first-step displacement, although not in a simple, addi-

tive manner; supination angle had an additional, minor influence (Fig. 3, D and E). On the level substrate, increasing adduction angle led to the largest performance increase, with supination angles of 30° and tail use resulting in modest improvements at lower adduction angles but offering minimal improvement over performance at the highest adduction angle (Fig. 3, B and D). At higher substrate angles with consequently lower granular yield forces, the role of the tail became dominant; effective locomotion without the tail was possible only at the highest adduction and lowest supination angles, but the use of the tail allowed locomotion over a wide range of limb kinematics (Fig. 3, C and E). In many of these cases, the use of the tail was the difference between success and failure [at $\theta = 20^\circ$, there were 15 failures among the 30 different configurations of ϕ and ψ (Fig. 3, D and E)]. Thus, the tail was not simply a uniform addition of propulsive force conferring a uniform advantage, as it did little to improve performance under near-optimal conditions. Instead, the tail had the greatest benefit when locomotion was otherwise compromised or ineffective as a result of low adduction angle or high substrate angle. A second set of trials

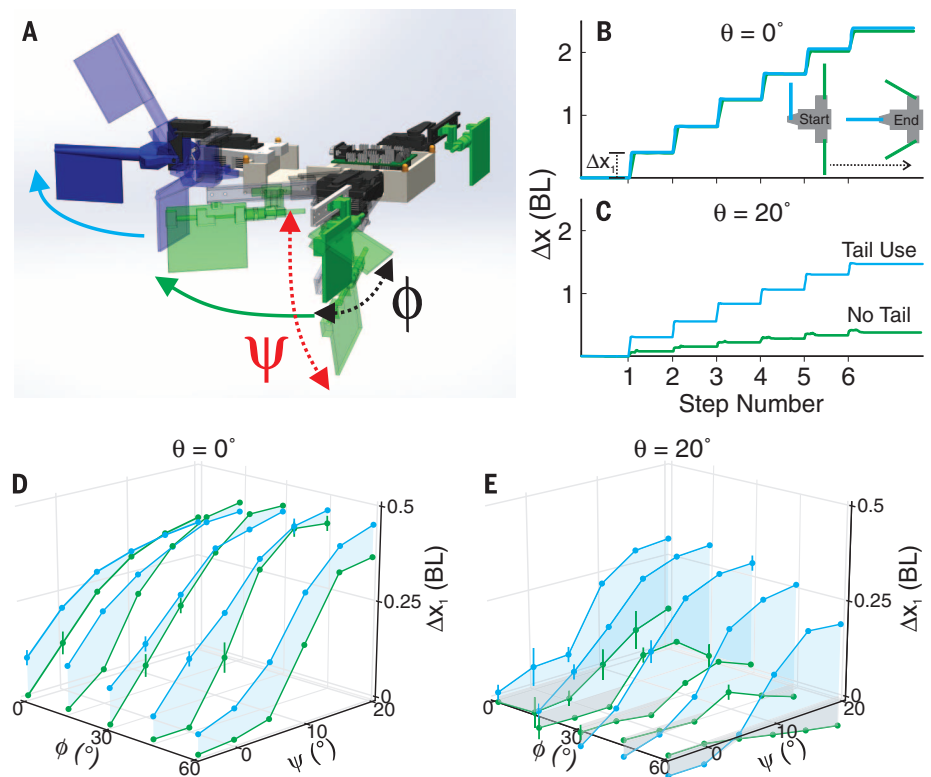


Fig. 3. Robophysical experiments on granular media at various substrate inclines (θ). (A) 3D model of MuddyBot, showing ranges of motion for limb retraction (green arrow, 60°) and tail motion (blue arrow, 90°). Limb adduction (ψ , -5° to 20° , where 0° is horizontal) and limb supination (ϕ , 0° to 60° , where 0° is vertical to the limb) are labeled, with other arrows showing directions of limb and tail motion during thrust phase. (B and C) Kinematics of a single trial of MuddyBot ($\phi = 15^\circ$, $\psi = 15^\circ$) moving for six cycles, without tail use (green) and with tail use (blue), on level ($\theta = 0^\circ$) (B) and inclined ($\theta = 20^\circ$) (C) poppy seeds. (D and E) First-step net displacement versus adduction and supination angles on $\theta = 0^\circ$ (D) and $\theta = 20^\circ$ (E) poppy seeds. Blue shading shows regions of identical supination angle for clarity. Vertical lines denote SD > 0.01 . Gray shading indicates negative values.

conducted using a different granular material showed qualitatively similar results [spherical plastic particles (table S1)], indicating that these results are robust to different granular media of different particle size and friction (figs. S2 and S5).

To gain insight into effective coordination of locomotor structures, we created a mathematical planar model of the robot using geometric

mechanics. This method, developed as a theoretical framework to elucidate principles of movement (27), describes how the self-deformation of the body (in our case, limb or tail movements) (Fig. 4A) generates net translation (or rotation) of the body. Geometric mechanics has been useful for understanding robot swimming (cyclic self-deformation due to traveling-wave body undulation) within granular media in which

inertial forces were small relative to frictional forces (28).

The geometric mechanics framework relies on construction of a “local connection” (34), which can be visualized as vector fields representing the link between small self-deformations (changes in the locomotor’s shape space, the set of internal shapes the mechanism can assume, here defined by planar limb and tail angles; Fig. 4A) and the resulting movement in world space (Fig. 4, D and E). For any given body configuration (a point in the diagrams in Fig. 4, D and E), the corresponding vector indicates the body deformation pattern that results in maximal forward movement. That is, if the robot begins from an arbitrary limb and tail angle combination (Fig. 4A), which corresponds to a horizontal and vertical location on the vector field (Fig. 4, D and E), a self-deformation parallel to the vector at that location will produce the greatest world-space incremental displacement, whereas self-deformations perpendicular to that vector will produce zero displacement. The overall pattern of a vector field allows visualization of how a time-varying pattern of self-deformations—represented as a path in the shape space—results in translation (or rotation). The net movement for a given sequence of limb and tail movements can be evaluated via a line integral in the vector field, with more effective motor patterns represented as paths that locally align more closely with vectors and pass through vectors of larger magnitudes (Fig. 4, D and E) (24).

Construction of local connection vector fields requires knowledge of how limb and tail segments experience drag forces. Because fundamental equations of motion for granular drag in the regime relevant to our robot studies do not exist, we generated the vector fields in Fig. 4, D and E, by empirically estimating the forces acting on a robot limb moving through granular media in plate drag experiments (figs. S3, S5, and S6) [assuming the material was continuously deforming and thus in the “frictional fluid” regime (33, 35)]. Similar to previous studies (5, 33, 35), the measured force was a function of the drag angle between the limb tangent and velocity vectors (Fig. 4B, inset), depth of intrusion into the media, and media incline, and was insensitive to speed (within the relevant range).

In such non-inertial limb- and tail-driven locomotion, the interaction between the granular media and the limb is governed by the ratio of the perpendicular thrust forces to parallel drag forces. These ratios collapsed to a single curve across inclines, depths (Fig. 4B), and granular media (fig. S5 and supplementary materials). This collapse suggests that the change in performance on granular slopes in the crutching locomotion may be a consequence of the effect of gravity on the body. Because our drag measurements were made in freshly prepared media, and because we could not model the possible interactions with the footprints of previous steps (8), we confined our analysis to the first step, as with the robot. Further, only high adduction angles were considered, so that we could avoid the effects of an accumulating pile of granular media at the front of the robot

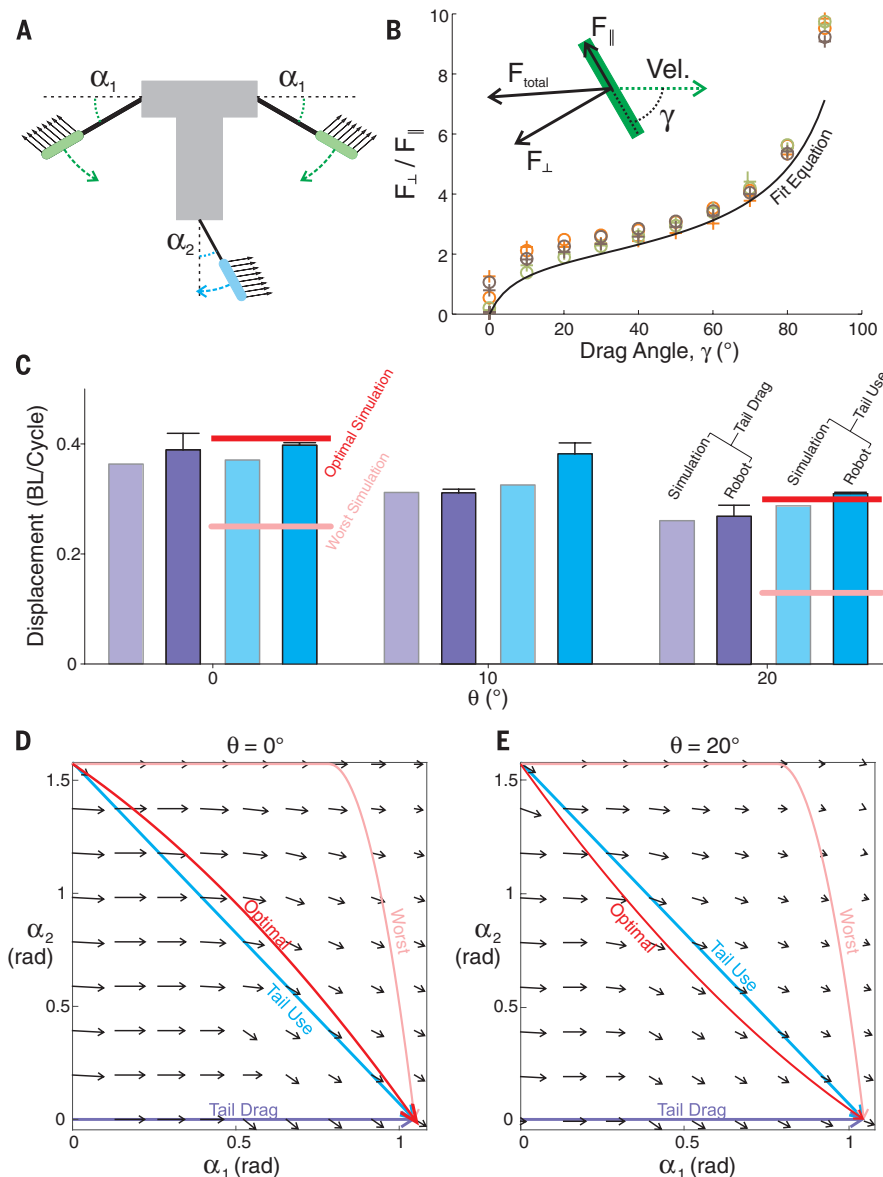


Fig. 4. Geometric mechanics model of MuddyBot locomotion. (A) A diagram of the simulation, showing the limb angle (α_1) and tail angle (α_2) as well as the reaction forces used to compute the local connection (see supplementary materials) between body deformation and body displacement. (B) The ratio of forces parallel and perpendicular to the limb surface during poppy seed drag experiments at various drag angles to the direction of motion, insertion depths, and substrate slopes. Intrusion depths are 1 cm (crosses) and 3 cm (circles), with $\theta = 0^\circ$ (brown), 20° uphill (orange), and 20° downhill (green). The black line represents the ratio of perpendicular and parallel equations (fitted independently; see supplementary materials). (C) First-step displacement (without slip) of the robot and simulation at all inclines ($\psi = 20^\circ$, $\phi = 0^\circ$), showing close agreement between the simulation and robot performance. Red and pink bars indicate the optimal and worst gaits, respectively. (D and E) Local connection vector field for $\theta = 0^\circ$ (D) and $\theta = 20^\circ$ (E) media, showing the limb only with tail dragging (purple) and tail gaits (light blue), as well as calculated optimal (red) and worst (pink) gaits.

when the body was insufficiently lifted. Additionally, when the tail was lifted clear of the media in robot experiments, the posterior motor and mounting structures intruded into and dragged through the media, resulting in an intrusion that was difficult to model; therefore, we simulated trials with the tail intruding into the media in the same configuration as at the end of tail-thrusting behavior, which yielded similar performance. To test these assumptions, we compared results to a subset of robot trials, and obtained good agreement between simulation and experiment (Fig. 4C and fig. S4).

The change in the patterns of the local connection vector fields revealed how limbs and tail could coordinate to produce movement (Fig. 4, C to E). For example, these fields demonstrated that the tail was not uniformly beneficial in all situations, nor even substantially beneficial in horizontal movement, in which the vertical component of the vectors (tail contribution) was small. However, as surface incline angle increased, the horizontal magnitudes of connection vectors decreased, indicating reduced efficacy of limb-only tail-dragging gaits (a horizontal path across the vector field). The relatively larger vertical component across more of the shape space indicated the increased importance of the tail to forward movement. The optimal gait for both inclines was close to the synchronous thrusting used by the robot and mudskipper, yielding similar displacements (Fig. 4, C to E); phase lag between initiation of limb and tail movement was suboptimal and, in one case per incline, yielded the worst possible gait (Fig. 4, D and E). Improper use of the tail resulted in substantially lower performance than simply allowing it to drag (Fig. 4, C to E). Additionally, the generally downward direction of the vectors in both fields demonstrate that purely tail-powered locomotion (a vertical path down the right of the vector field) can produce forward motion, as seen in some extant fish (12).

Our results from a biological analog of early tetrapods and robophysical and mathematical models demonstrate that the tail can play an important role in limb-driven crutching locomotion on inclined granular substrates by making locomotors more robust to suboptimal kinematics and substrate conditions. This suggests that the sizable, well-ossified (and presumably well-muscled) tails of early tetrapods (15–17), originally used for swimming, may have been co-opted to promote reliable locomotion over challenging substrates, providing an exaptation (36) that facilitated their invasion of land. Although evidence of tail use is absent among the few fossil trackways attributed to early tetrapods (37, 38), tail use might be evident in trackways formed on inclined shores.

REFERENCES AND NOTES

- J. A. Clack, *Gaining Ground: The Origin and Evolution of Tetrapods* (Indiana Univ. Press, 2002).
- E. B. Daeschler, N. H. Shubin, F. A. Jenkins Jr., *Nature* **440**, 757–763 (2006).
- A. Blicek et al., *Geol. Soc. London Spec. Publ.* **278**, 219–235 (2007).
- N. Gravish, P. B. Umbanhowar, D. I. Goldman, *Phys. Rev. Lett.* **105**, 128301 (2010).
- H. Marvi et al., *Science* **346**, 224–229 (2014).
- F. Qian et al., *Bioinspir. Biomim.* **10**, 056014 (2015).
- C. Li, P. B. Umbanhowar, H. Komsuoglu, D. E. Koditschek, D. I. Goldman, *Proc. Natl. Acad. Sci. U.S.A.* **106**, 3029–3034 (2009).
- N. Mazouchova, P. B. Umbanhowar, D. I. Goldman, *Bioinspir. Biomim.* **8**, 026007 (2013).
- J. Davenport, A. K. M. A. Matin, *J. Fish Biol.* **37**, 175–184 (1990).
- A. G. Johnels, *Oikos* **8**, 122 (1957).
- C. M. Pace, A. C. Gibb, *J. Exp. Biol.* **214**, 530–537 (2011).
- C. M. Pace, A. C. Gibb, *J. Fish Biol.* **84**, 639–660 (2014).
- A. Jusufi, D. I. Goldman, S. Revzen, R. J. Full, *Proc. Natl. Acad. Sci. U.S.A.* **105**, 4215–4219 (2008).
- T. Libby et al., *Nature* **481**, 181–184 (2012).
- E. Jarvik, *Medd. Gronl.* **114**, 1–90 (1952).
- E. Jarvik, *The Devonian Tetrapod Ichthyostega* (Indiana Univ. Press, 1996).
- M. I. Coates, *Trans. R. Soc. Edinb. Earth Sci.* **87**, 363–421 (1996).
- R. W. Blob, *Paleobiology* **27**, 14–38 (2001).
- M. A. Ashley-Ross, S. T. Hsieh, A. C. Gibb, R. W. Blob, *Integr. Comp. Biol.* **53**, 192–196 (2013).
- S. E. Pierce, J. A. Clack, J. R. Hutchinson, *Nature* **486**, 523–526 (2012).
- S. E. Pierce, J. R. Hutchinson, J. A. Clack, *Integr. Comp. Biol.* **53**, 209–223 (2013).
- E. M. Standen, T. Y. Du, H. C. E. Larsson, *Nature* **513**, 54–58 (2014).
- S. M. Kawano, R. W. Blob, *Integr. Comp. Biol.* **53**, 283–294 (2013).
- V. A. Harris, *Proc. Zool. Soc. London* **134**, 107–135 (1960).
- B. O. Swanson, A. C. Gibb, *J. Exp. Biol.* **207**, 4037–4044 (2004).
- J. Aguilari, D. I. Goldman, *Nat. Phys.* **12**, 278 (2016).
- A. Shapere, F. Wilczek, *Phys. Rev. Lett.* **58**, 2051–2054 (1987).
- R. L. Hatton, Y. Ding, H. Choset, D. I. Goldman, *Phys. Rev. Lett.* **110**, 078101 (2013).
- N. Mitarai, F. Nori, *Adv. Phys.* **55**, 1–45 (2006).
- S. S. Sharpe, R. Kuckuk, D. I. Goldman, *Phys. Biol.* **12**, 046009 (2015).
- H. Askari, K. Kamrin, <http://arxiv.org/abs/1510.02966> (2015).
- K. Nishikawa et al., *Integr. Comp. Biol.* **47**, 16–54 (2007).
- C. Li, T. Zhang, D. I. Goldman, *Science* **339**, 1408–1412 (2013).
- S. D. Kelly, R. M. Murray, *J. Robot. Syst.* **12**, 417–431 (1995).
- R. D. Maladen, Y. Ding, C. Li, D. I. Goldman, *Science* **325**, 314–318 (2009).
- S. J. Gould, E. S. Vrba, *Paleobiology* **8**, 4–15 (1982).
- J. Clack, *Palaeoogeogr. Palaeoclimatol. Palaeoecol.* **130**, 227–250 (1997).
- S. Curth, M. S. Fischer, J. A. Nyakatura, *Ichnos* **21**, 32–43 (2014).

ACKNOWLEDGMENTS

Supported by NSF grants PoLS PHY-1205878, PHY-1150760, and CMMI-1361778. Army Research Office (ARO) grant W911NF-11-1-0514, and the ARL MAST CTA (D.I.G.); ARO Robotics CTA and NSF National Robotics Initiative IIS-1426655 (H.C.); NSF grants IOS-0517340 and IOS-0817794 (R.W.B.); GT UROP and the GT PURA Travel Grant (B.M.); a Clemson University Wade Stackhouse Fellowship, NSF award DBI-1300426, and the University of Tennessee, Knoxville (S.M.K.); and the U.S. Department of Defense, Air Force Office of Scientific Research, National Defense Science and Engineering Graduate (NDSEG) Fellowship, 32 CFR 168a (P.E.S.). The authors declare no conflicts of interest. Data are available from the corresponding author upon request.

SUPPLEMENTARY MATERIALS

www.sciencemag.org/content/353/6295/154/suppl/DC1
Materials and Methods
Supplementary Text
Figs. S1 to S6
Table S1
Movies S1 to S6
References (39, 40)

16 December 2015; accepted 26 May 2016
10.1126/science.aaf0984

ROBOTICS

Phototactic guidance of a tissue-engineered soft-robotic ray

Sung-Jin Park,¹ Mattia Gazzola,^{2,*} Kyung Soo Park,^{3,4,†} Shirley Park,^{5,‡} Valentina Di Santo,⁶ Erin L. Blevins,^{6,§} Johan U. Lind,¹ Patrick H. Campbell,¹ Stephanie Dauth,¹ Andrew K. Capulli,¹ Francesco S. Pasqualini,¹ Seungkuk Ahn,¹ Alexander Cho,¹ Hongyan Yuan,^{1||} Ben M. Maoz,¹ Ragu Vijaykumar,⁵ Jeong-Woo Choi,^{3,4} Karl Deisseroth,^{5,7} George V. Lauder,⁶ L. Mahadevan,^{2,8} Kevin Kit Parker^{1,4,¶}

Inspired by the relatively simple morphological blueprint provided by batoid fish such as stingrays and skates, we created a biohybrid system that enables an artificial animal—a tissue-engineered ray—to swim and phototactically follow a light cue. By patterning dissociated rat cardiomyocytes on an elastomeric body enclosing a microfabricated gold skeleton, we replicated fish morphology at $1/_{10}$ scale and captured basic fin deflection patterns of batoid fish. Optogenetics allows for phototactic guidance, steering, and turning maneuvers. Optical stimulation induced sequential muscle activation via serpentine-patterned muscle circuits, leading to coordinated undulatory swimming. The speed and direction of the ray was controlled by modulating light frequency and by independently eliciting right and left fins, allowing the biohybrid machine to maneuver through an obstacle course.

Bioinspired design, as applied to robotics, aims at implementing naturally occurring features such as soft materials, morphologies, gaits, and control mechanisms in artificial settings in order to improve performance (1–4). For example, recent soft-robotics studies raised awareness on the importance of

material properties (3, 4), shifting the focus from rigid elements to soft materials, whereas other investigations report successful mimicry of gaits or morphological features inspired by insects (5, 6), fish (7, 8), snakes (9), salamanders (10), and cheetahs (11). Although recent advances have the promise of bridging the performance gap with animals,



Tail use improves performance on soft substrates in models of early vertebrate land locomotors

Benjamin McInroe, Henry C. Astley, Chaohui Gong, Sandy M. Kawano, Perrin E. Schiebel, Jennifer M. Rieser, Howie Choset, Richard W. Blob and Daniel I. Goldman (July 7, 2016)
Science **353** (6295), 154-158. [doi: 10.1126/science.aaf0984]

Editor's Summary

This copy is for your personal, non-commercial use only.

- Article Tools** Visit the online version of this article to access the personalization and article tools:
<http://science.sciencemag.org/content/353/6295/154>
- Permissions** Obtain information about reproducing this article:
<http://www.sciencemag.org/about/permissions.dtl>

Science (print ISSN 0036-8075; online ISSN 1095-9203) is published weekly, except the last week in December, by the American Association for the Advancement of Science, 1200 New York Avenue NW, Washington, DC 20005. Copyright 2016 by the American Association for the Advancement of Science; all rights reserved. The title *Science* is a registered trademark of AAAS.



Supplementary Materials for

Tail use improves performance on soft substrates in models of early vertebrate land locomotors

Benjamin McInroe, Henry C. Astley, Chaohui Gong, Sandy M. Kawano, Perrin E. Schiebel,
Jennifer M. Rieser, Howie Choset, Richard W. Blob, Daniel I. Goldman*

*Corresponding author. Email: daniel.goldman@physics.gatech.edu

Published 8 July 2016, *Science* **353**, 154 (2016)
DOI: 10.1126/science.aaf0984

This PDF file includes:

Materials and Methods

Supplementary Text

Figs. S1 to S6

Table S1

Captions for movies S1 to S6

References

Other supplementary material for this manuscript includes the following:

Movies S1 to S6

1 Materials and Methods

1.1 Mudskipper Experiments

We selected the mudskipper fish (*Periophthalmus barbaratus*) (Fig. 1C,D) as a living functional analog for early tetrapods, because it employs a bilaterally symmetric crutching gait hypothesized to be similar to the gait used by some early walkers [20,21]. Six mudskippers (maximum anterior-posterior length: 10.5 ± 3.9 cm, mass: 6.5 ± 5.2 g) were acquired from commercial vendors. All data from mudskippers were collected under Clemson University IACUC Animal Use Protocol 2013-065. The test arena was a bed of dry oolite sand (Table S1) (51×28 cm²) which was tilted to 0°, 10°, or 20°. Tracks were smoothed away between trials while the fish rested, and the sand was stirred to reset compaction state. Dry granular media was used to facilitate repeatability of trials. Mudskippers were placed in the arena and encouraged (via non-contacting hand movements) to move along the long axis of the bed (uphill if inclined) while being recorded at 100 frames per second using two Phantom HSV cameras (model: V5.1) from lateral and dorsal views. All individuals were presented with all inclines, though not all performed crutching (as opposed to no movement or jumping out of the bed). Order of angle presentation was not completely randomized due to the need for fixed experimental setups at each incline and differing individual availability. The location of the eye was digitized from the vertical view, and the forward displacement (Δx) of the mudskipper was measured, with the net displacement projected orthogonal to the axis of inclination of the trackway and normalized by body length. Presence or absence of propulsive tail use was scored for each cycle (Total cycles: 0° N=77, 10° N=70, 20° N=55).

1.2 Robot Experiments

To systematically evaluate the performance impact of variation in specific locomotor features observed in mudskippers, we developed a limb- and tail-driven robophysical model inspired by mudskipper morphology and movements (Fig. 1E, 3A). The central body of the robot was composed of 3D printed plastic, which served to anchor four LED lights for tracking, a Lynxmotion SSC-32 Servo Controller, and the limbs. Each pectoral limb was actuated by two HS-M7990TH Hitec servomotors, with the most proximal servomotor controlling vertical motion of the limb (ab/adduction) while the distal servomotor controlled horizontal motion (pro/retraction). Flippers (7.75×6.5 cm²) were mounted to the end of arm supports extending from the distal servomotor, and could be manually positioned and locked at a range of supination angles from 0° (perpendicular to the substrate) to 60°. The proximal motor of the tail was a HS-M7990TH Hitec servomotor which powered lateral movements, while tail vertical movement was actuated by a HS-A-5076HB Hitec servomotor. Theoretical calculations based on the geometric mechanics model suggest a maximum shoulder torque of 0.6 N-m, while the M7990TH Hitec servomotors are capable of generating up to 4.3 N-m, indicating motor performance could be maintained without degradation across the range of gravitational loads to which the robot was exposed.

Each arm was 21 cm in length (measured from the most proximal motor axis to the distal edge of limb), and the arms were separated by 13 cm for a total “armspan” of 55 cm. Tail fin dimensions were identical to those of the pectoral limbs, with a total tail length of 20 cm and

located 22 cm posterior to the pectoral limbs. The antero-posterior location of the center of mass was 10 cm from the anterior edge of the robot, 6 cm behind the horizontal axis of rotation of the arms. Relationships between servomotor pulse widths and joint angles were verified by direct measurement, as were the angles of manually positioned joints. Signals were sent using a custom program written in Python (available in data repository).

The tail moved through a 90° range of motion, starting perpendicular to the sagittal plane and ending parallel to it, alternating between starting on the left and on the right. Pectoral limbs started perpendicular to the sagittal plane and retracted 60° simultaneously. Tail use was simultaneous with pectoral limb movement, as in mudskippers. The duration for both limb and tail movement was 2 seconds; faster movements produced unreliable robot kinematics. During the repositioning ("swing phase") between cycles, the tail remained planted in its final position while the pectoral limbs were lifted clear of the substrate, protracted to the starting angle, and planted again, after which the tail was lifted, repositioned and planted in preparation for the next cycle. This prevented slipping backwards at high bed inclines, and was similar to the pattern observed in the mudskippers.

The robot experiments were performed on level and inclined substrates (1.2 x 1.8 m² bed), using two different types of dry granular media, poppy seeds and spherical plastic particles (Sup. Table 1) of 10 cm depth, manually reset between trials to erase tracks. These substrates were chosen because the oolite sand would have destroyed the servomotors, while poppy seeds can be readily pulverized within the mechanism and the plastic particles are too large to get inside the motor housing. The substrates differed by approximately an order of magnitude in diameter (0.7 mm and 6 mm, respectively) and had substantially different frictional properties, leading to angles of repose of 36° and 21°, respectively. However, the very highest inclines were not accessible by the robot, as the yield strength of the material at these slopes was so low that the slightest movements would cause the robot to slip to the bottom of the bed. Therefore, poppy seed trials were conducted at 0°, 10°, or 20°, while spherical plastic particle trials were conducted only at 0° and 10°. Experiments on spherical plastic particles showed similar results to those on poppy seeds, and are shown in Fig. S2. In all cases, media was of sufficient depth to prevent the robot from interacting with the sides or bottom of the container via boundary effects. Robot motion was recorded at 120 fps using a top-down Point Grey Grasshopper camera mounted to the bed and controlled via a LabView interface, for three trials of six steps each per condition (adduction, supination, tail use, and incline). This program isolated and recorded the positions of the four LEDs in the field of view, the average of which was then used to determine displacement of the robot. Each step displacement was calculated from these positions over time, without backwards slipping during swing phase.

Robot configurations included arm adduction (ψ) from -5° to 20° (0° is horizontal) in 5° increments and limb supination (ϕ) from 0° to 60° (0° is vertical to the limb) in 15° increments, resulting in 30 limb configurations, all of which were tested with and without tail use for each substrate and incline. Each combination of substrate, incline, tail use, and limb configuration was tested for a full six cycles a total of three times.

1.3 Drag Measurements

Granular drag measurements were performed using a 3D printed plastic limb (flat plate) of the same dimensions and material as those from Muddybot. The limb was partially submerged into the granular media, with intrusion depth measured from undisturbed granular surface to the bottom edge of the limb (Fig. S3A). In these experiments, the limb was moved a distance of 21.5 cm at a speed of 1 cm/s for intrusion depths of 1 and 3 cm. None of the granular media used in these tests exhibited speed dependence over the range of yielding media speeds encountered by the robot and mudskipper (5-10 cm/s), as noted below and shown in Fig. S6. All tests were performed in both level granular media and 20° media incline, both uphill and downhill. The forces normal and tangential to the plate in the direction of motion were measured as a function of drag angle γ , defined as the angle between the tangent vector to the limb face and the direction of displacement. An air fluidized bed of 152 cm length and 53 cm width was used to control the initial state of the media. The poppy seeds filled the bed to a depth of 8 cm, sufficient to prevent boundary effects acting between the floor and the intruder. Before each trial, air was passed through the porous rigid floor of the bed to fluidize the poppy seed grains, allowing them to behave like a fluid and thereby erase prior deformations due to yielding. Airflow was then turned off and the grains allowed to settle into a loosely packed state. For trials on the 20° slopes, two linear actuators (Firgelli Automation FA-200-L-12) were used to slowly change bed angle once the media had settled.

A rotation stage (Newport 481-A) was used to manually adjust the angle of the intruder relative to the direction of motion (drag angle, γ) from 0° to 90° in 10° increments. The granular drag forces acting on the limb were measured using a 6-axis force/torque sensor (Mini40, ATI industrial) mounted between the intruder and the rotation stage. Data were collected at 1000Hz and the sensor resolved the force measurement into components parallel, F_{\parallel} , and perpendicular, F_{\perp} , to the limb face. Intruder displacement was achieved using a Copley linear actuator (Copley Controls) attached to a linear stage (Igus DryLin) on which the intruder, rotation stage, and force sensor were mounted.

We used the following previously suggested empirical functions to fit the data: [8,39]

$$F_{\perp}(\gamma) = C \sin(\gamma) \quad (1)$$

$$F_{\parallel}(\gamma) = A \cos(\gamma) + B(1 - \sin(\gamma)) + F_0 \quad (2)$$

Using MATLAB *lsqnonlin* function we found values for the fitting parameters (with 95% confidence intervals) for a limb intruded 1 cm in level media to be:

$$C = 0.66(0.64, 0.69)N \quad (3)$$

$$A = 0.27(0.20, 0.33)N \quad (4)$$

$$B = -0.32(-0.38, -0.26)N \quad (5)$$

$$F_0 = 0.09(0.07, 0.12)N \quad (6)$$

To assess the effect of hand smoothing on the properties of the poppy seeds we used a 6-axis robotic arm (Denso VS087A2-AV6-NNN-NNN) to drag the 3D printed plastic muddybot limb over a distance of 20 cm at 1 cm/s. Forces were resolved using a 6-axis force/torque

sensor (Nano43, ATI Industrial). The poppy seeds were filled to a depth of approximately 15 cm in an air-fluidized bed 44 cm in length and 29 cm in width, large enough to prevent boundary effects due to the walls or floor of the bed. We used both fluidization-prepared loose-packed poppy seeds—the same preparation technique as used in the above drag experiments—as well as hand-smoothed poppy seeds—the preparation technique used in the muddybot robot trials. We collected three trials each at drag angles of 90° (plate face perpendicular to the direction of motion) and 45° for a total of 12 trials (6 fluidized and 6 hand-smoothed). We found that hand-smoothing did not affect the material response to drag, and the anisotropy (ratio of perpendicular to parallel force) of the manually reset trials agreed with that of the fluidized trials (Fig. S5).

To determine the nature of the material response to drag for the different granular media used in our locomotion experiments, we used the same setup and dragged the intruder 20 cm at a speed of 1 cm/s. Drag angle was varied from 0-90° in 10° increments, similar to the motion used to determine the empirical functions (1) and (2). We tested the spherical plastic particles used in the robot trials using the muddybot flipper intruder and the oolite sand used in the mudskipper trials using a 3x3x0.01 cm³ aluminum plate. This Al plate is comparable in scale with the mudskipper (anterior-posterior length 10.5 ± 3.9 cm). The oolite sand was prepared using fluidization while the plastic particles, which could not be fluidized using the current setup, were hand-smoothed between trials. In the plastic particles, the drag angle was varied from 0–90° in 10° increments at an intrusion depth of 3 cm. We chose this intrusion as 3 cm intrusion is in line with the intrusion depths observed in muddybot trials. We also collected trials at approximately 1 cm depth for 20°, 40°, 60°, and 80° drag angles and find that the force anisotropies for the two intrusions are equivalent (Fig. S5). In the oolite sand, the drag angle was varied from 0–90° in 10° increments at an intrusion depth of 5 mm. This agrees with the limb intrusions observed in the mudskipper experiments. As with the plastic particles, we also tested the four drag angles (20°, 40°, 60°, and 80°) at 1 cm intrusion to confirm that the anisotropy is independent of depth at these ranges and find good agreement both with the anisotropy of oolite sand intruded to 5 mm as well as with the anisotropy of the poppy seeds. The relationship between anisotropy and drag angle of the spherical plastic particles has a similar shape to that of the poppy seeds and oolite sand, however the magnitude of the anisotropy increases more quickly as the angle increases. We believe this can be attributed to the low friction between the plastic flipper and plastic beads as compared to that between the flipper and poppy seeds or Al plate and oolite sand.

We also verified that the granular response to drag is insensitive to velocity. The poppy seeds and spherical plastic particles were again tested with the flipper intruder and the oolite sand using the 3x3x0.01 cm³ Al plate. Material was prepared the same way as in the material response trials. The flipper was intruded to a depth of 1cm in the poppy seeds, 3 cm in the plastic particles, and 5 mm in the oolite sand. In poppy seeds and oolite sand, perpendicular forces were measured for intruder speeds from 1 to 20 cm/s in 1 cm/s increments and at 0.5 cm/s. In plastic particles, the forces were measured at speeds of 5, 10, 15, and 20 cm/s. We find that force is insensitive to speed for speeds relevant to the locomotion tested (Fig. S6). Calculations of maximum yielding sand movement speed based on the robot movements ((21 cm * $\pi/3$) / (2 sec) = 11 cm/s) and digitizing the interface between yielding sand and both the pectoral and tail fins (~5-10 cm/s) yielded similar speeds for the granular media in high-yield

cases, and both were well within the range of speeds for which force is speed-insensitive in all media (Fig. S6).

1.4 Simulations

To investigate how limb-tail coordination affects locomotor performance, we developed a mathematical model of the MuddyBot using techniques from geometric mechanics [28]. The dimensions of the model were based on the MuddyBot, and the reaction forces experienced on the limbs and tail were computed using the empirically determined force relations described in Equations (1) and (2). The model was two dimensional, since the vertical position of the robot was only relevant to whether a given body segment contacted the ground and thus experienced granular forces. During the propulsion phase in the high adduction state we simulated, only the flippers and tail contacted the media. Due to the complexity of the shape of the rear of the MuddyBot and the consequent difficulty of effective drag calculations, we used an alternative configuration in which the tail dragged behind the robot in a rigid posture, making the posterior intruder a flat plate and, consequently, more amenable to analysis. This resulted in slightly less drag than during the tail-lifted experiments, but otherwise identical results. We denoted the body velocity of the robot (the velocity viewed in the frame of the body which is located at the CoM of the robot body assuming massless appendages and aligned with the axis of symmetry of the body, see Figure S7 for a diagram) as $\xi = (\mathbf{g}_b^{-1}\dot{\mathbf{g}}_b)^\vee$, where \mathbf{g}_b is a homogeneous transformation matrix and under standard convention [41] also labels the robot body frame, and the “unhat” operator performs,

$$\begin{bmatrix} 0 & -\xi^\theta & \xi^x \\ \xi^\theta & 0 & \xi^y \\ 0 & 0 & 0 \end{bmatrix}^\vee = \begin{bmatrix} \xi^x \\ \xi^y \\ \xi^\theta \end{bmatrix}. \quad (7)$$

Given ξ and joint velocities $\dot{\alpha}$, the velocities of an appendage $\mathbf{v}_i = (\mathbf{g}_i^{-1}\dot{\mathbf{g}}_i)^\vee$ (again, where each \mathbf{g}_i is a homogeneous transformation matrix and also labels the frame of the i^{th} appendage with $i = \{l, r, t\}$) with respect to the substrate frame \mathbf{g}_w can be computed as,

$$\mathbf{v}_i = \begin{bmatrix} \cos(\theta'_i) & \sin(\theta'_i) & x'_i \sin(\theta'_i) - y'_i \cos(\theta'_i) \\ -\sin(\theta'_i) & \cos(\theta'_i) & x'_i \cos(\theta'_i) + y'_i \sin(\theta'_i) \\ 0 & 0 & 1 \end{bmatrix} \xi + \mathbf{J}_i \dot{\alpha} \quad (8)$$

where (x'_i, y'_i, θ'_i) denotes the position and orientation of an appendage with respect to the body frame of the robot, and the matrix is the adjoint operator [41] which maps velocity of the body in the body frame to the local frame of the appendage, and \mathbf{J}_i denotes the Jacobian matrix that maps $\dot{\alpha}$ to the velocity of appendages relative to the body frame of the robot. The angle of motion of the appendages relative to the substrate (γ_i) was computed as,

$$\gamma_i = \tan^{-1} \left(\frac{v_i^y}{v_i^x} \right) \quad (9)$$

where v_i^x and v_i^y respectively denote the velocity parallel and perpendicular to an appendage (see inset in Figure 4B in main text), and γ_i is used to calculate reaction forces \mathbf{F}_i on appendages via Equations (1) and (2) above. Reaction forces on appendages were then mapped to the frame of the robot body using

$$\mathbf{F}_i^b = \begin{bmatrix} \cos(\theta_i') & \sin(\theta_i') & y_i' \\ \sin(\theta_i') & \cos(\theta_i') & -x_i' \\ 0 & 0 & 0 \end{bmatrix} \mathbf{F}_i. \quad (10)$$

We assumed the robot moved quasi-statically, and the total forces experienced on the system summed to zero at any instant of time,

$$\sum \mathbf{F}_i^b + \sin(\beta) [0 \quad -mg \quad 0]^T = \mathbf{0} \quad (11)$$

where mg denotes the gravitational force on the robot and β denotes substrate incline angle. The only unknown variable in Equation (11) was ξ which was solved using a nonlinear root finding algorithm. Solving for Equation (11) at different commanded joint velocities allowed us to numerically derive the local connection using the method described in [28],

$$\xi = \mathbf{A}(\alpha)\dot{\alpha} \quad (12)$$

where $\mathbf{A}(\alpha)$ is the local connection, a linear approximation to the mapping from $\dot{\alpha}$ to ξ .

The local connection describes how internal body deformations generate external movements. The three rows of the local connection are related to robot motion respectively in the lateral, forward and rotational directions. Because we were primarily interested in studying movement in the forward direction, we focused our study on the second row of the local connection. The second row (motion in the forward direction) of $\mathbf{A}(\alpha)$ defines a ‘‘connection vector field’’, which graphically shows how infinitesimal limb-tail movements affect displacements in the forward direction. The vectors in the connection vector field denote the directions in which shape changes would lead to most effective forward movement, the magnitude of which was annotated by the length of the vector. For example, at a given α , a shape velocity perpendicular to the vector field would produce zero forward velocity, whereas a shape velocity along the vector field would result in a large forward velocity.

A kinematic program (coordinated limb-tail movement) can be graphically represented as a continuous path in a vector field. Because only small off-axis rotations were observed in the MuddyBot experiments, we used the integral of forward body velocity ξ_y as an approximation to the actual forward displacement. In general, paths corresponding to effective kinematic programs follow along the ‘‘flows’’ of the connection vector fields. Therefore, the structures of connection vector fields can be used for understanding how kinematics impact locomotion.

We used the connection vector field to find coordinated limb-tail coordinations that can produce maximum forward displacement per gait cycle. To do so, we first discretized the shape space into a 21×21 two-dimensional grid. Every node on the grid represents one static

shape of the MuddyBot, and an edge connecting two nodes represents the corresponding joint motion. We assigned a score to each edge with a value equal to the forward displacement that would result from executing this joint motion. We assumed unidirectional motions of both limbs and tail during the robot movement—limb angles always increase and tail angle always decreases during a step. An effective kinematic strategy was then found as the path on this grid that had the maximal accumulated score. Using the Bellman-Ford algorithm, paths with largest accumulated scores (optimal gait) and lowest accumulated scores (worst gait) were efficiently identified [40].

1.5 Supplementary Table

Media	Diameter (mm)	Solid Density $\frac{g}{cm^3}$	Angle of Stability
Oolite sand	0.25–0.75	1.52	37°
Poppy seeds	0.7±0.2	1.2	36°
Spherical plastic particles	5.87±0.06	1.03	21°

Table S1: Properties of granular media used in this study.

1.6 Supplementary Movie Captions

Supplementary Movies 1 and 2 show a mudskipper moving on slopes of 0° and 20°, respectively, from dorsal and lateral views, at 100 frames per second. Videos slowed 4x.

Supplementary Movies 3 and 4 show Muddybot moving on level media using 0° supination and 20° adduction without and with tail use, respectively, in real-time. Scale bars are projections from the bed surface.

Supplementary Movies 5 and 6 show Muddybot moving on 20° inclined media using 0° supination and 20° adduction without and with tail use, respectively, in real-time. Scale bars are projections from the bed surface.

1.7 Supplementary Programs & Data

Supplementary programs and data are archived at the following URL:
<http://hdl.handle.net/1853/54827>

These data include the geometric mechanics programs (Matlab scripts), the Solidworks parts and assembly files for Muddybot, the Muddybot control program (Python 2.7), the Muddybot data (tab-delimited text files) with instructions, and the mudskipper digitized data (with instructions).

1.8 Supplementary Figures

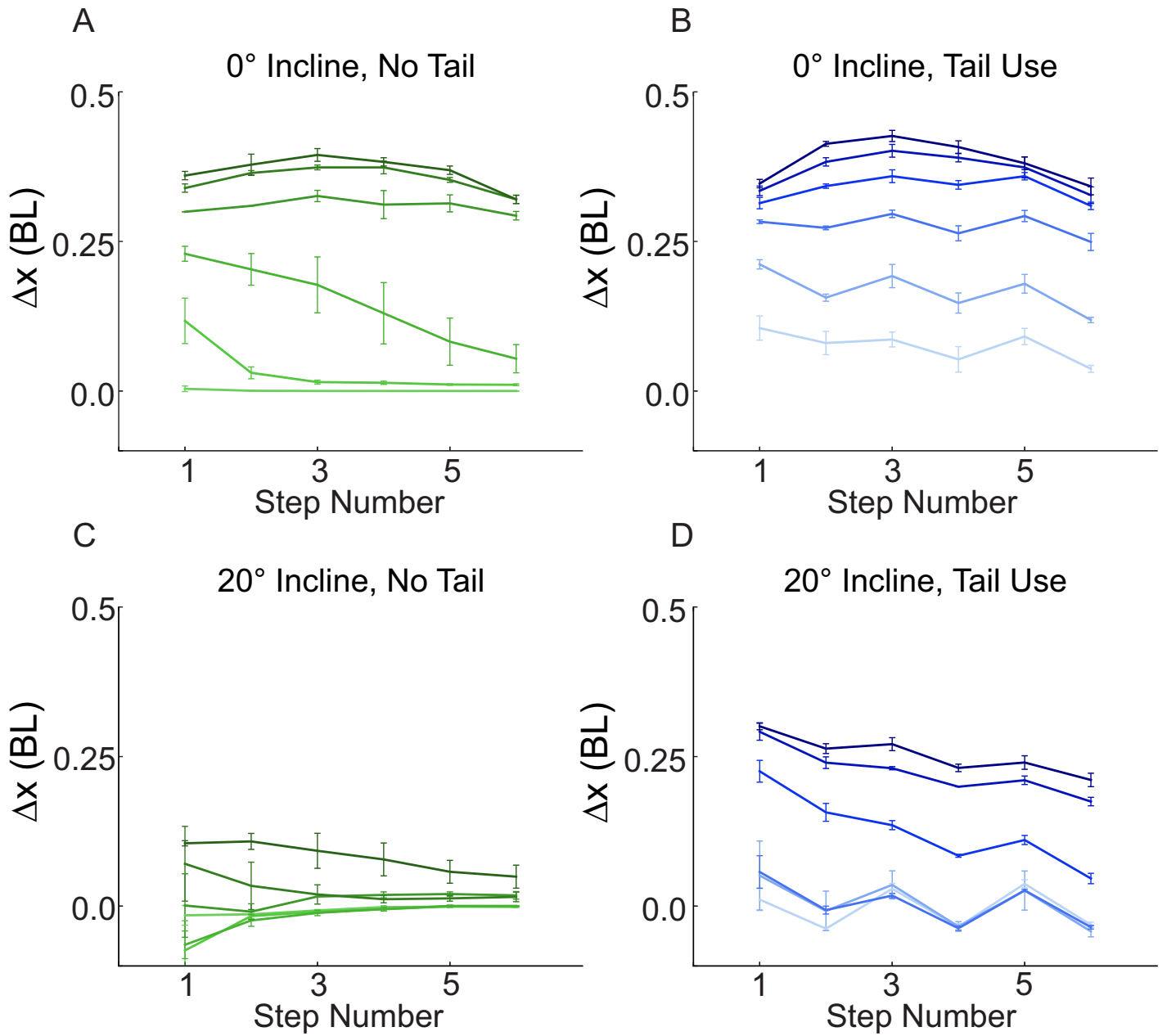


Figure 1: **Displacement per step in poppy seeds for various robot experiments.** (A) Displacement in each of the 6 steps of a robot ($\phi = 0^\circ$) without tail use, on horizontal media. Color indicates adduction angle (ψ), with the darkest green being 20° , and the lightest being -5° . (B) Displacement in each of the 6 steps of a robot ($\phi = 0^\circ$) with tail use. Color indicates adduction angle (ψ), with the darkest blue being 20° , and the lightest being -5° . (C) Displacement in each of the 6 steps of a robot ($\phi = 0^\circ$) without tail use, on 20° inclined media. (D) Displacement in each of the 6 steps of a robot ($\phi = 0^\circ$) with tail use, on 20° inclined media.

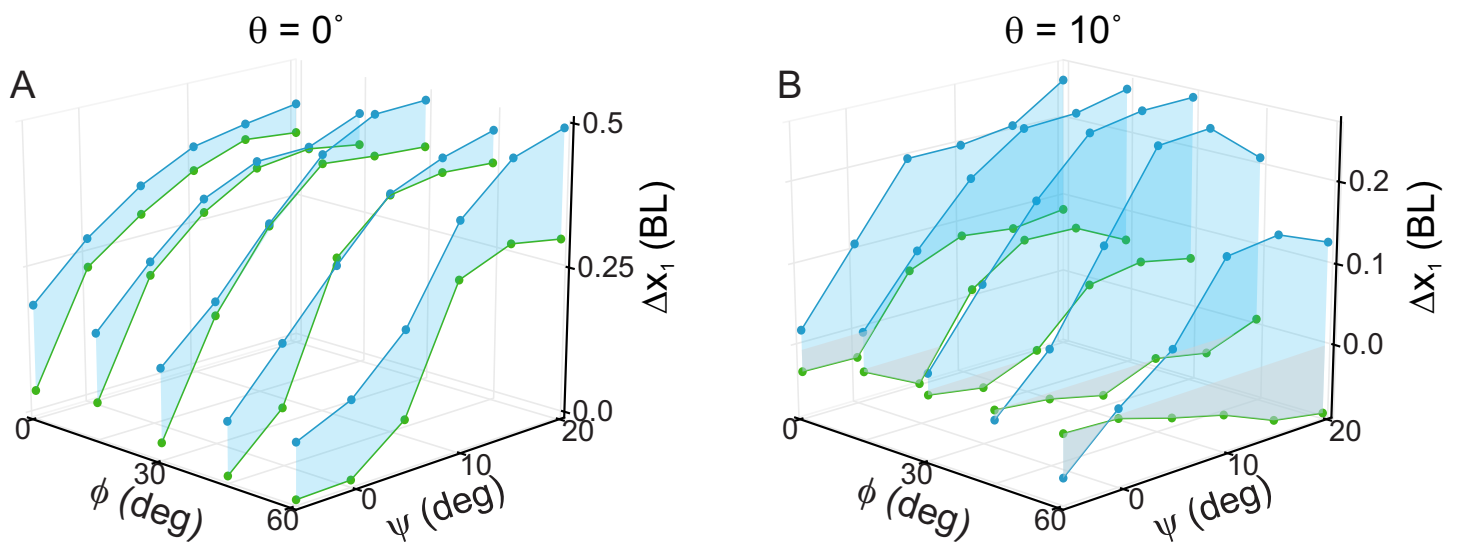


Figure 2: **Robot performance on spherical plastic particles.** Blue markers indicate trials with tail use, green markers indicate trials without tail use. (A) First-step net displacement vs adduction and supination angles on $\theta = 0^\circ$ inclined spherical plastic particles. Blue shading shows regions of identical supination angle for clarity. (B) First-step net displacement vs adduction and supination angles on $\theta = 10^\circ$ spherical plastic particles. Grey shading indicates negative values.

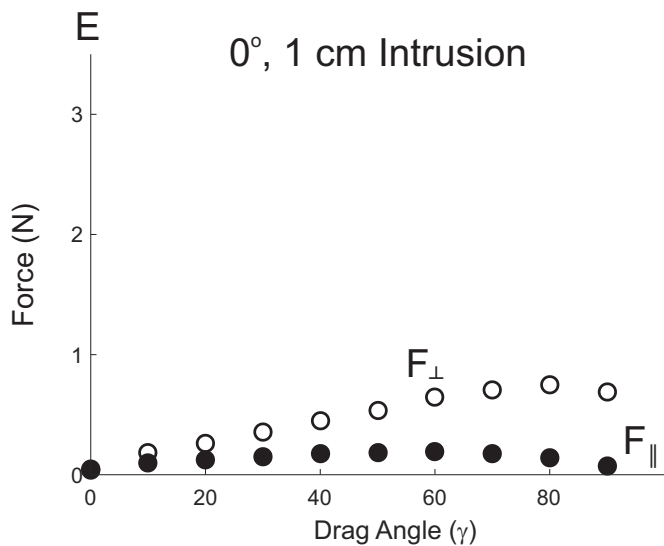
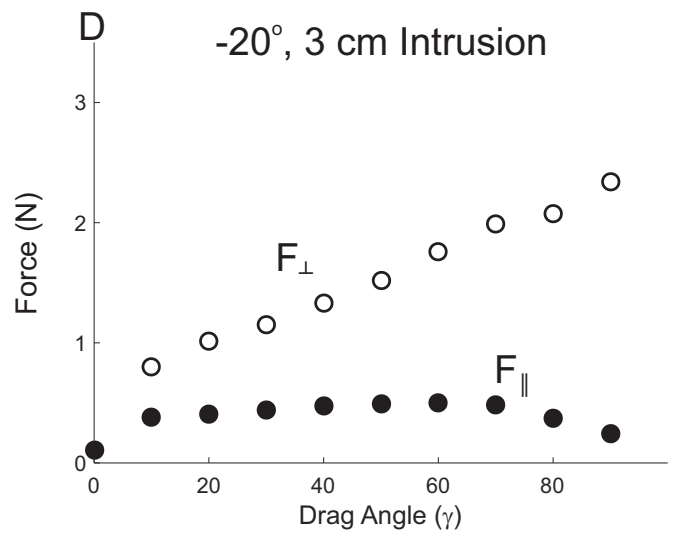
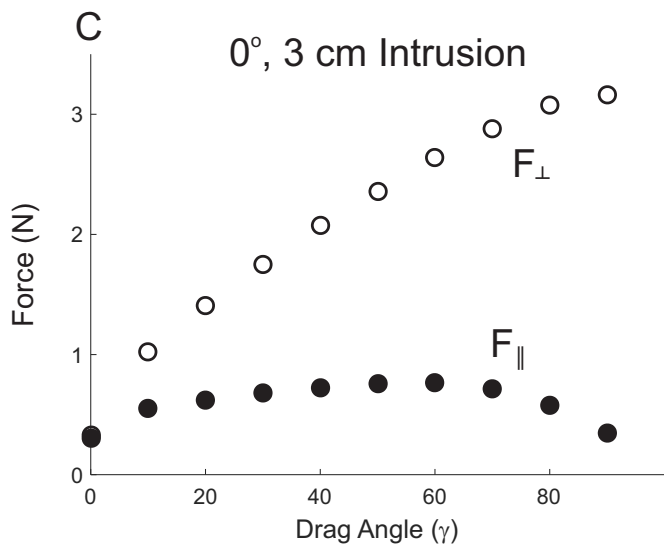
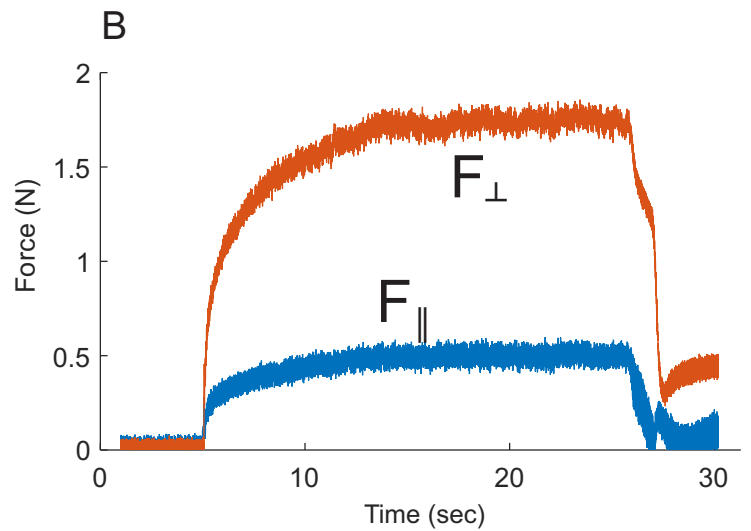
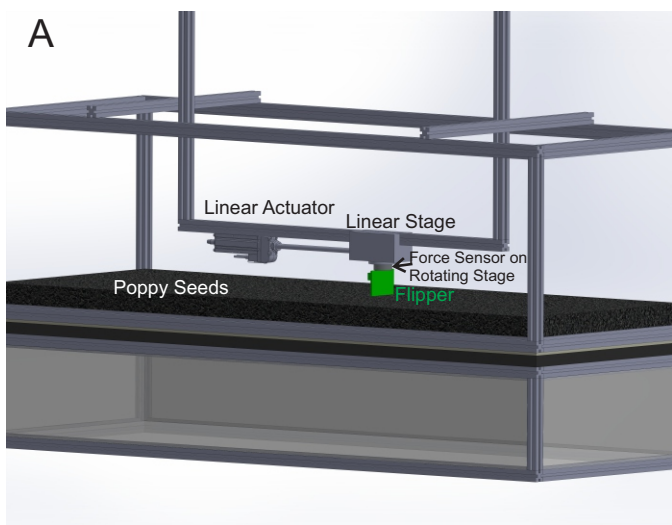


Figure 3: Perpendicular and parallel forces during drag experiments in poppy seeds. (A) Experimental setup for drag characterization. (B) Parallel and perpendicular forces over time in an example trial (insertion depth = 3 cm, bed angle = 20° downhill, limb angle = 60°). (C) Forces (perpendicular = hollow, parallel = solid) for various drag angles at a 3 cm insertion depth and 0° bed angle. (D) Forces (perpendicular = hollow, parallel = solid) for various drag angles at a 3 cm insertion depth and 20° downhill bed angle. (E) Forces (perpendicular = hollow, parallel = solid) for various drag angles at a 1 cm insertion depth and 0° bed angle.

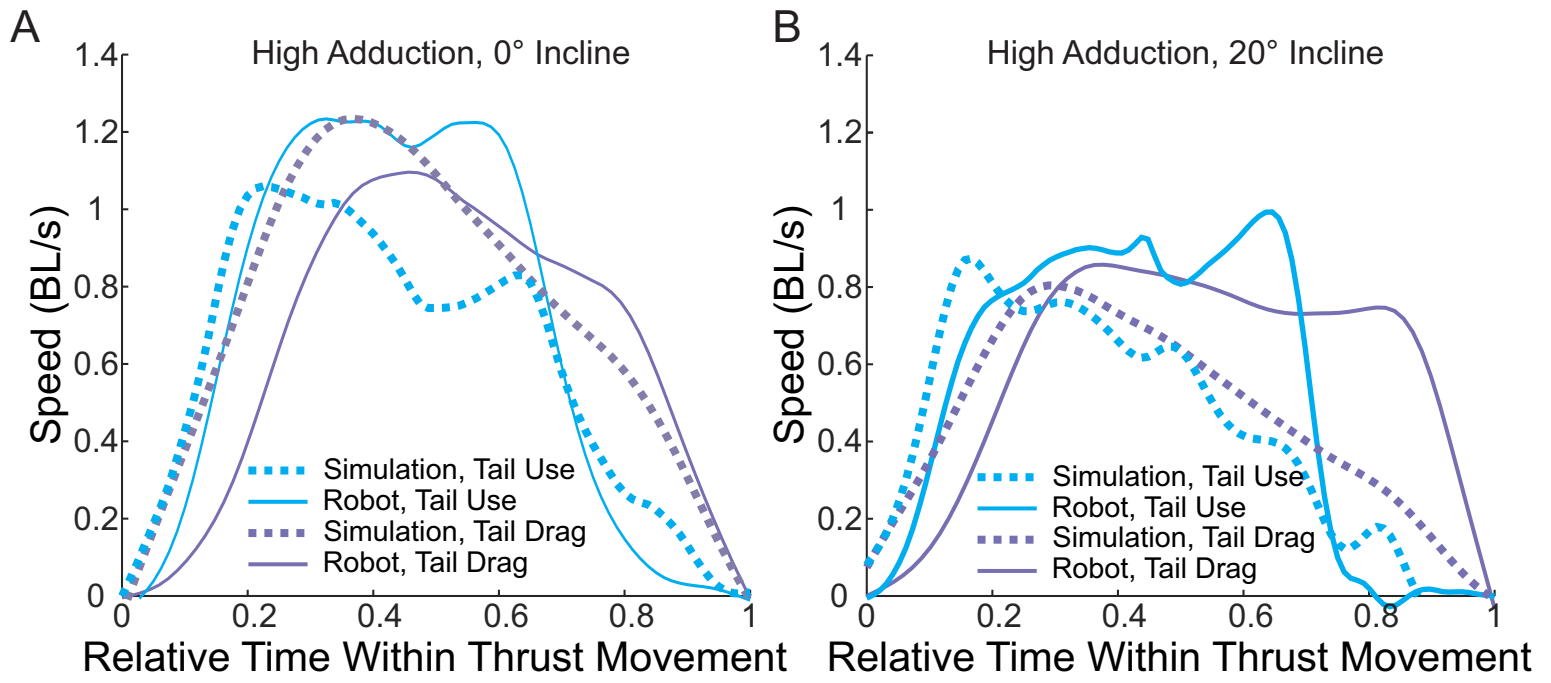


Figure 4: **Instantaneous velocities (in body lengths per cycle) of the simulated and real Muddybot, with and without tail use** A) 0° incline and B) 20° incline. Robots typically achieved greater velocity late in the cycle, likely due to substrate accumulation behind the limbs, which was not modeled.

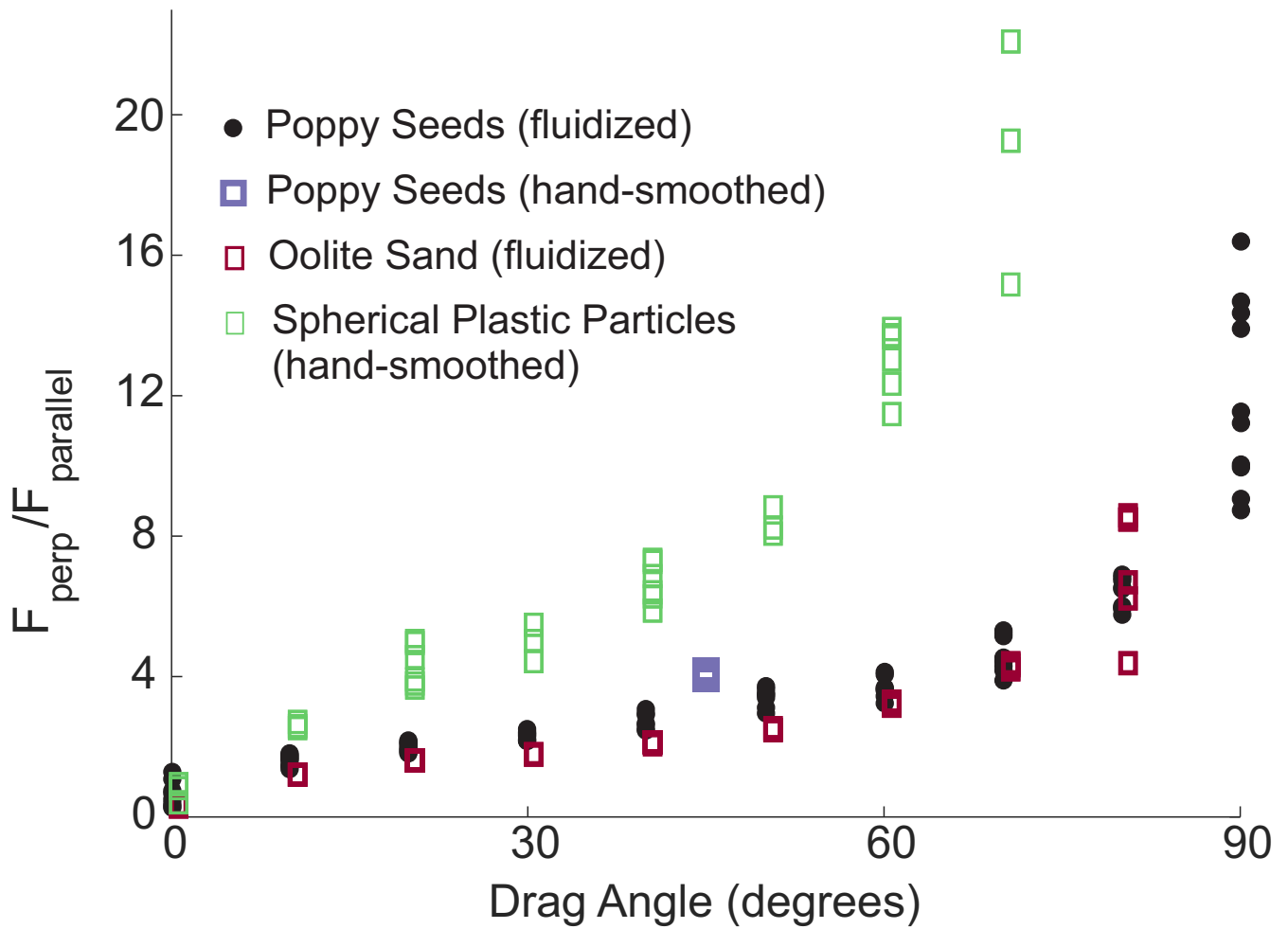


Figure 5: **Drag experiments across media types and preparation techniques.** The ratio of perpendicular and parallel forces for poppy seeds prepared via fluidization (as in Fig. 4B), hand-smoothed poppy seeds, oolite sand, and spherical plastic particles. The plastic particles depart from the curve, due to low parallel forces as a consequence of low friction between the particles and flipper. Values at high drag angles are not plotted for all media as the parallel forces near zero.

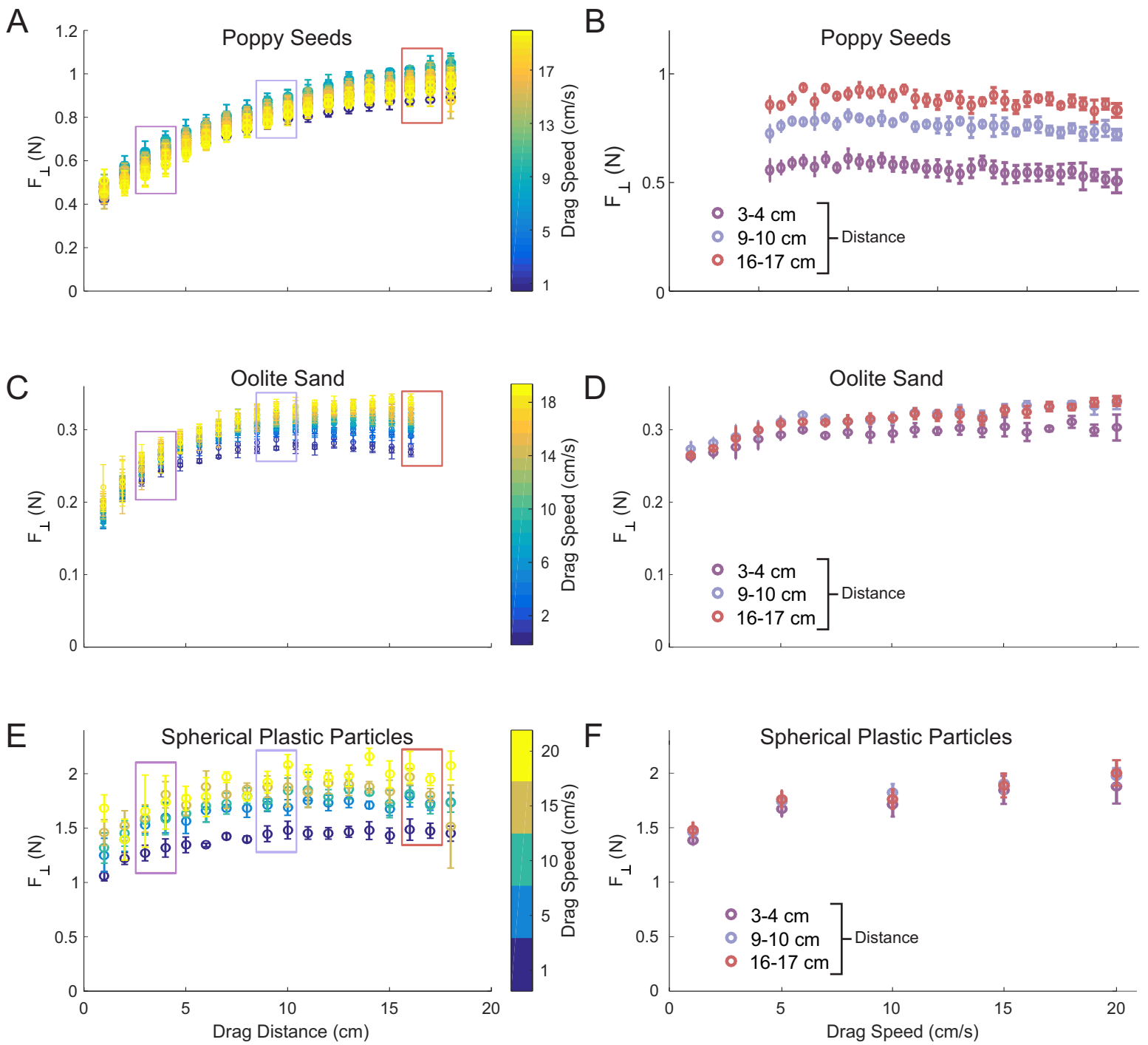


Figure 6: **Drag experiments across media types and speeds.** Perpendicular force as a function of distance (A, C, E) and speed (B, D, F) of intruder movement in three materials: (A & B) poppy seeds (prepared by fluidization), (C & D) oolite sand (prepared by fluidization), and (E & F) spherical plastic particles (prepared by hand-smoothing). Boxes in A, C, & E indicate the distance intervals used in B, D, & F, with corresponding colors.

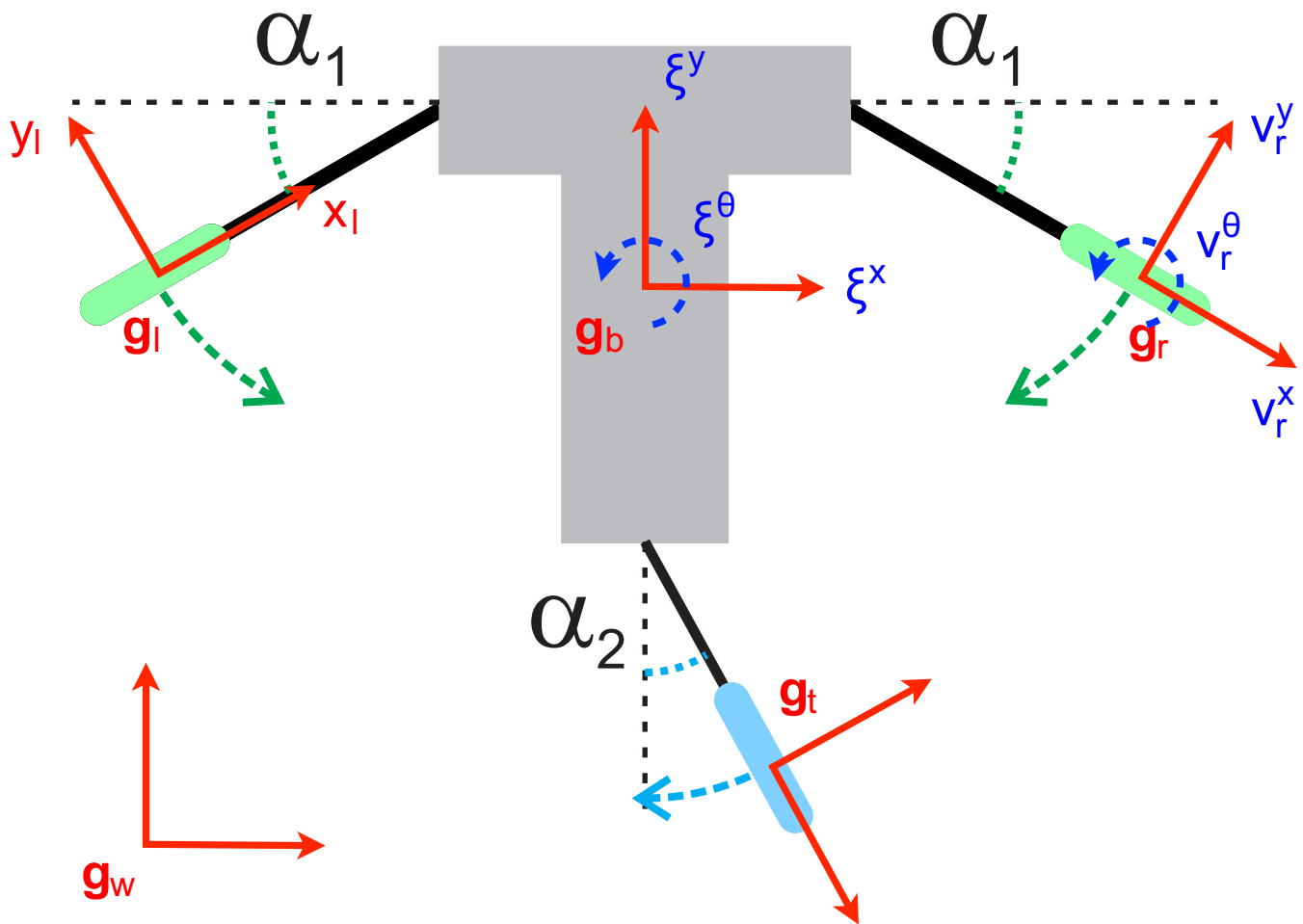


Figure 7: **Diagram of Geometric Mechanics model of MuddyBot, showing coordinate frames and velocities used in the calculations.**

Joint angles are α_1 and α_2 , while \mathbf{g} denotes the reference frames of body, left limb, right limb, tail, and world. Components of ξ show velocity of the body in its reference frame, and components of \mathbf{v} denotes velocity of the limb in its reference frame, both with superscripts x , y , and θ to denote movements and rotations in local reference frames.

References

1. J. A. Clack, *Gaining Ground: The Origin and Evolution of Tetrapods* (Indiana Univ. Press, 2002).
2. E. B. Daeschler, N. H. Shubin, F. A. Jenkins Jr., A Devonian tetrapod-like fish and the evolution of the tetrapod body plan. *Nature* **440**, 757–763 (2006). [10.1038/nature04639](https://doi.org/10.1038/nature04639) [Medline](#)
[doi:10.1038/nature04639](https://doi.org/10.1038/nature04639)
3. A. Blicek, G. Clement, H. Blom, H. Lelievre, E. Luksevics, M. StreeL, J. Thorez, G. C. Young, The biostratigraphical and palaeogeographical framework of the earliest diversification of tetrapods (Late Devonian). *Geol. Soc. London Spec. Pub.* **278**, 219–235 (2007).
[doi:10.1144/SP278.10](https://doi.org/10.1144/SP278.10)
4. N. Gravish, P. B. Umbanhowar, D. I. Goldman, Force and flow transition in plowed granular media. *Phys. Rev. Lett.* **105**, 128301 (2010). [Medline](#)
[doi:10.1103/PhysRevLett.105.128301](https://doi.org/10.1103/PhysRevLett.105.128301)
5. H. Marvi, C. Gong, N. Gravish, H. Astley, M. Travers, R. L. Hatton, J. R. Mendelson 3rd, H. Choset, D. L. Hu, D. I. Goldman, Sidewinding with minimal slip: Snake and robot ascent of sandy slopes. *Science* **346**, 224–229 (2014). [Medline](#) [doi:10.1126/science.1255718](https://doi.org/10.1126/science.1255718)
6. F. Qian, T. Zhang, W. Korff, P. B. Umbanhowar, R. J. Full, D. I. Goldman, Principles of appendage design in robots and animals determining terradynamic performance on flowable ground. *Bioinspir. Biomim.* **10**, 056014 (2015). [Medline](#)
[doi:10.1088/1748-3190/10/5/056014](https://doi.org/10.1088/1748-3190/10/5/056014)
7. C. Li, P. B. Umbanhowar, H. Komsuoglu, D. E. Koditschek, D. I. Goldman, Sensitive dependence of the motion of a legged robot on granular media. *Proc. Natl. Acad. Sci. U.S.A.* **106**, 3029–3034 (2009). [Medline](#) [doi:10.1073/pnas.0809095106](https://doi.org/10.1073/pnas.0809095106)
8. N. Mazouchova, P. B. Umbanhowar, D. I. Goldman, Flipper-driven terrestrial locomotion of a sea turtle-inspired robot. *Bioinspir. Biomim.* **8**, 026007 (2013). [Medline](#)
[doi:10.1088/1748-3182/8/2/026007](https://doi.org/10.1088/1748-3182/8/2/026007)
9. J. Davenport, A. K. M. A. Matin, Terrestrial locomotion in the climbing perch, *Anabas testudineus* (Bloch) (Anabantidea, Pisces). *J. Fish Biol.* **37**, 175–184 (1990).
[doi:10.1111/j.1095-8649.1990.tb05938.x](https://doi.org/10.1111/j.1095-8649.1990.tb05938.x)
10. A. G. Johnels, The mode of terrestrial locomotion in *Clarias*. *Oikos* **8**, 122 (1957).
[doi:10.2307/3564996](https://doi.org/10.2307/3564996)
11. C. M. Pace, A. C. Gibb, Locomotor behavior across an environmental transition in the ropefish, *Erpetoichthys calabaricus*. *J. Exp. Biol.* **214**, 530–537 (2011). [Medline](#)
[doi:10.1242/jeb.047902](https://doi.org/10.1242/jeb.047902)
12. C. M. Pace, A. C. Gibb, Sustained periodic terrestrial locomotion in air-breathing fishes. *J. Fish Biol.* **84**, 639–660 (2014). [Medline](#) [doi:10.1111/jfb.12318](https://doi.org/10.1111/jfb.12318)

13. A. Jusufi, D. I. Goldman, S. Revzen, R. J. Full, Active tails enhance arboreal acrobatics in geckos. *Proc. Natl. Acad. Sci. U.S.A.* **105**, 4215–4219 (2008). [Medline](#)
[doi:10.1073/pnas.0711944105](https://doi.org/10.1073/pnas.0711944105)
14. T. Libby, T. Y. Moore, E. Chang-Siu, D. Li, D. J. Cohen, A. Jusufi, R. J. Full, Tail-assisted pitch control in lizards, robots and dinosaurs. *Nature* **481**, 181–184 (2012). [Medline](#)
[doi:10.1038/nature10710](https://doi.org/10.1038/nature10710)
15. E. Jarvik, On the fish-like tail in the ichthyostegid stegocephalians, with descriptions of a new stegocephalian and a new crossopterygian from the Upper Devonian of East Greenland. *Medd. Gronl.* **114**, 1–90 (1952).
16. E. Jarvik, *The Devonian Tetrapod Ichthyostega* (Indiana Univ. Press, 1996).
17. M. I. Coates, The Devonian tetrapod *Acanthostega gunnari* Jarvik: Postcranial anatomy, basal tetrapod interrelationships and patterns of skeletal evolution. *Trans. R. Soc. Edinb. Earth Sci.* **87**, 363–421 (1996). [doi:10.1017/S0263593300006787](https://doi.org/10.1017/S0263593300006787)
18. R. W. Blob, Evolution of hindlimb posture in nonmammalian therapsids: Biomechanical tests of paleontological hypotheses. *Paleobiology* **27**, 14–38 (2001).
[doi:10.1666/0094-8373\(2001\)027<0014:EOHPIN>2.0.CO;2](https://doi.org/10.1666/0094-8373(2001)027<0014:EOHPIN>2.0.CO;2)
19. M. A. Ashley-Ross, S. T. Hsieh, A. C. Gibb, R. W. Blob, Vertebrate land invasions-past, present, and future: An introduction to the symposium. *Integr. Comp. Biol.* **53**, 192–196 (2013). [Medline](#) [doi:10.1093/icb/ict048](https://doi.org/10.1093/icb/ict048)
20. S. E. Pierce, J. A. Clack, J. R. Hutchinson, Three-dimensional limb joint mobility in the early tetrapod *Ichthyostega*. *Nature* **486**, 523–526 (2012). [Medline](#)
21. S. E. Pierce, J. R. Hutchinson, J. A. Clack, Historical perspectives on the evolution of tetrapodomorph movement. *Integr. Comp. Biol.* **53**, 209–223 (2013). [Medline](#)
[doi:10.1093/icb/ict022](https://doi.org/10.1093/icb/ict022)
22. E. M. Standen, T. Y. Du, H. C. E. Larsson, Developmental plasticity and the origin of tetrapods. *Nature* **513**, 54–58 (2014). [Medline](#) [doi:10.1038/nature13708](https://doi.org/10.1038/nature13708)
23. S. M. Kawano, R. W. Blob, Propulsive forces of mudskipper fins and salamander limbs during terrestrial locomotion: Implications for the invasion of land. *Integr. Comp. Biol.* **53**, 283–294 (2013). [Medline](#) [doi:10.1093/icb/ict051](https://doi.org/10.1093/icb/ict051)
24. V. A. Harris, On the locomotion of the mud-skipper *Periophthalmus koelreuteri* (Pallas): (Gobiidae). *Proc. Zool. Soc. London* **134**, 107–135 (1960).
[doi:10.1111/j.1469-7998.1960.tb05921.x](https://doi.org/10.1111/j.1469-7998.1960.tb05921.x)
25. B. O. Swanson, A. C. Gibb, Kinematics of aquatic and terrestrial escape responses in mudskippers. *J. Exp. Biol.* **207**, 4037–4044 (2004). [Medline](#) [doi:10.1242/jeb.01237](https://doi.org/10.1242/jeb.01237)
26. J. Aguilar, D. I. Goldman, Robophysical study of jumping dynamics on granular media. *Nat. Phys.* **12**, 278–283 (2015). [doi:10.1038/nphys3568](https://doi.org/10.1038/nphys3568)

27. A. Shapere, F. Wilczek, Self-propulsion at low Reynolds number. *Phys. Rev. Lett.* **58**, 2051–2054 (1987). [Medline doi:10.1103/PhysRevLett.58.2051](#)
28. R. L. Hatton, Y. Ding, H. Choset, D. I. Goldman, Geometric visualization of self-propulsion in a complex medium. *Phys. Rev. Lett.* **110**, 078101 (2013). [Medline doi:10.1103/PhysRevLett.110.078101](#)
29. N. Mitarai, F. Nori, Wet granular materials. *Adv. Phys.* **55**, 1–45 (2006). [doi:10.1080/00018730600626065](#)
30. S. S. Sharpe, R. Kuckuk, D. I. Goldman, Controlled preparation of wet granular media reveals limits to lizard burial ability. *Phys. Biol.* **12**, 046009 (2015). [Medline doi:10.1088/1478-3975/12/4/046009](#)
31. H. Askari, K. Kamrin, <http://arxiv.org/abs/1510.02966> (2015).
32. K. Nishikawa, A. A. Biewener, P. Aerts, A. N. Ahn, H. J. Chiel, M. A. Daley, T. L. Daniel, R. J. Full, M. E. Hale, T. L. Hedrick, A. K. Lappin, T. R. Nichols, R. D. Quinn, R. A. Satterlie, B. Szymik, Neuromechanics: An integrative approach for understanding motor control. *Integr. Comp. Biol.* **47**, 16–54 (2007). [Medline doi:10.1093/icb/icm024](#)
33. C. Li, T. Zhang, D. I. Goldman, A terradynamics of legged locomotion on granular media. *Science* **339**, 1408–1412 (2013). [Medline doi:10.1126/science.1229163](#)
34. S. D. Kelly, R. M. Murray, Geometric phases and robotic locomotion. *J. Robot. Syst.* **12**, 417–431 (1995). [doi:10.1002/rob.4620120607](#)
35. R. D. Maladen, Y. Ding, C. Li, D. I. Goldman, Undulatory swimming in sand: Subsurface locomotion of the sandfish lizard. *Science* **325**, 314–318 (2009). [Medline doi:10.1126/science.1172490](#)
36. S. J. Gould, E. S. Vrba, Exaptation—a missing term in the science of form. *Paleobiology* **8**, 4–15 (1982). [doi:10.1017/S0094837300004310](#)
37. J. Clack, Devonian tetrapod trackways and trackmakers; a review of the fossils and footprints. *Palaeogeogr. Palaeoclimatol. Palaeoecol.* **130**, 227–250 (1997). [doi:10.1016/S0031-0182\(96\)00142-3](#)
38. S. Curth, M. S. Fischer, J. A. Nyakatura, Ichnology of an extant belly-dragging lizard—analogy to early reptile locomotion? *Ichnos* **21**, 32–43 (2014). [doi:10.1080/10420940.2013.877006](#)
39. R. D. Maladen, Y. Ding, P. B. Umbanhowar, A. Kamor, D. I. Goldman, Mechanical models of sandfish locomotion reveal principles of high performance subsurface sand-swimming. *J. R. Soc. Interface* **8**, 1332–1345 (2011). [doi:10.1098/rsif.2010.0678](#)
40. R. Bellman, *On a Routing Problem* (RAND Corporation, 1956).

41. R. M. Murray, Z. Li, S. S. Sastry, *A Mathematical Introduction to Robotic Manipulation* (CRC Press, 1994).